

Multi-Wave Coherent Control of a Solid State Single Emitter

F. Fras,^{1,2,3,*} Q. Mermillod,^{1,2} G. Nogues,^{1,2} C. Hoarau,^{1,2} C. Schneider,⁴ M. Kamp,⁴ S. Höfling,^{4,5} W. Langbein,⁶ and J. Kasprzak^{1,2,†}

¹*Univ. Grenoble Alpes, F-38000 Grenoble, France*

²*CNRS, Institut Néel, F-38000 Grenoble, France*

³*IPCMS UMR 7504, CNRS and Université de Strasbourg, Strasbourg, France*

⁴*Technische Physik and Wilhelm Conrad Röntgen Research Center for Complex Material Systems, Universität Würzburg, Germany*

⁵*SUPA, School of Physics and Astronomy, University of St Andrews, St Andrews, KY16 9SS, United Kingdom*

⁶*Cardiff University School of Physics and Astronomy, The Parade, Cardiff CF24 3AA, United Kingdom*

Coherent control of individual two-level systems (TLSs) is at the basis of any implementation of quantum information. An impressive level of control is now achieved using nuclear^{1,2}, vacancies^{3,4} and charge spins^{5,6}. Manipulation of bright exciton transitions in semiconductor quantum dots (QDs) is less advanced, principally due to the sub-nanosecond dephasing⁷. Conversely, owing to their robust coupling to light, one can apply tools of nonlinear spectroscopy⁸ to achieve all-optical command. Here, we report on the coherent manipulation of an exciton via multi-wave mixing. Specifically, we employ three resonant pulses driving a single InAs QD. The first two induce a four-wave mixing (FWM) transient, which is projected onto a six-wave mixing (SWM) depending on the delay and area of the third pulse, in agreement with analytical predictions. Such a switch enables to demonstrate the generation of SWM on a single emitter and to engineer the spectro-temporal shape of the coherent response originating from a TLS. These results pave the way toward multi-pulse manipulations of solid state qubits via implementing the NMR-like control schemes⁹ in the optical domain.

An appealing strategy to realize optically controlled quantum networks in solid state, is to coherently couple distant TLSs - like bright exciton transitions in QDs - via photons confined in microcavities^{10,11} or propagating in waveguides^{12–15}. The efficient retrieval and manipulation of coherent responses from single excitons is mandatory for assessing the properties of such solid state qubits and demonstrating the coherence transfer between them. In this context, substantial progress has been made by the introduction of the heterodyne spectral interferometry technique⁸ to measure four-wave mixing (FWM) from individual excitons in various nanostructures^{11,16–19}. Yet, measuring on single strongly-confined excitons in InAs QDs remains challenging and has not been previously achieved. This is due to their small dipole moment μ and the resulting required high resonant amplitudes of the three fields; $\mathcal{E}_1, \mathcal{E}_2, \mathcal{E}_3$, employed to drive the measured FWM polarization, being proportional to $\mu^4 \mathcal{E}_1^* \mathcal{E}_2 \mathcal{E}_3$ and higher order terms with the same phase dependence on the fields.

Here, the retrieval and manipulation of wave-mixing

signals from single InAs QDs is accomplished by embedding them in a low-Q planar semiconductor microcavity²⁰, as detailed in Supplementary Fig.S2. Such a semiconductor hetero-structure provides an intracavity field enhancement of $\sqrt{Q} \simeq 13$ at the QDs position, whilst offering spectral matching of the photonic mode with femto-second laser pulses. This cavity-enhanced driving allows reducing the resonant excitation intensity, required to induce the FWM, by a factor around $Q^{3/2} \simeq 2200$. In consequence, the retrieval efficiency of wave-mixing signals from single excitons is improved by two orders of magnitude with respect to previous experiments on bare QDs^{8,19}. In this work, we employ such wave-mixing responses to realize a novel scheme for ultrafast coherent control of optically active TLSs. We demonstrate gating of their coherent emission, by converting the FWM polarization into the SWM one. We show engineering of the FWM spectral response, also acting on the global spectral lineshape of a TLS. Details regarding the current experimental configuration are given in Supplementary Fig.S1.

For the purpose of the experiment described in this Letter, we require an optically active TLS in a solid. In InAs QDs, this is the case of negatively charged excitons (trions)²¹, where the level structure can be trimmed down to two levels (disregarding spin degeneracy): the ground and excited states corresponding to the presence of an electron and a trion in the QD, respectively, as depicted in Fig.1 a. We have therefore used a sample which is intentionally n-doped²⁰ with a Silicon δ -layer located in the cavity spacer. To illustrate the coherent response of trions, we present in Fig.1 a the spectral interferogram detected at the FWM frequency $2\Omega_2 - \Omega_1$, as detailed in the Supplementary Material. Based on series of interferograms, we construct the FWM hyperspectral imaging¹⁸, as exemplified in Fig.1 b. Therein, the brightest, localized peaks correspond primarily to the FWM generated by trions. Such imaging is employed to determine spatial and spectral position of QDs. Also it enables a detailed statistical analysis on excitonic complexes, as exemplified for biexcitons in Supplementary Fig.S3.

We first retrieve the required parameters to infer and model the optical response of single emitters in a solid. The three-beam FWM spectroscopy offers direct access to coherence and population dynamics in the TLS. To probe the population dynamics, we detect the time-integrated FWM at the $\Omega_3 + \Omega_2 - \Omega_1$

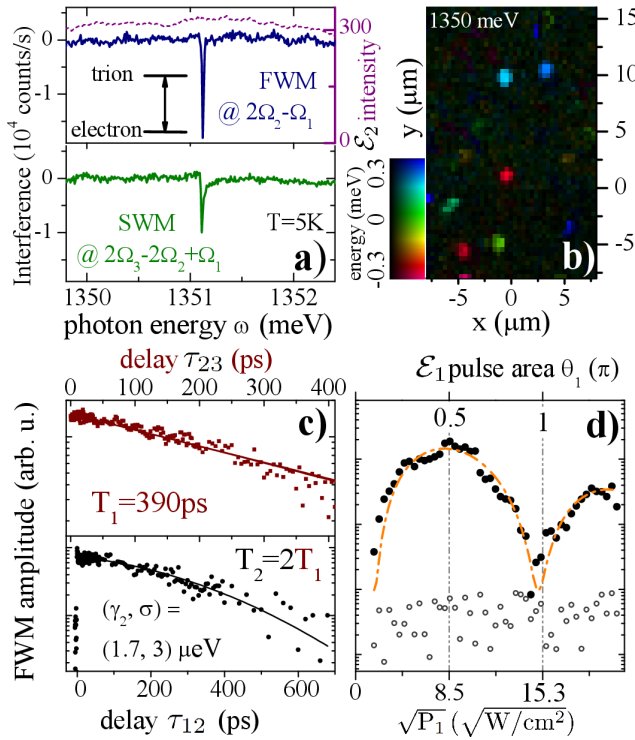


FIG. 1. Wave mixing spectroscopy of individual negative trions in InAs QDs embedded in a low-Q microcavity. a) Interferograms of four-wave mixing (FWM) of a single trion for $2\Omega_2 - \Omega_1$, $\tau_{12} = 0.5$ ps and pulse areas $(\theta_1, \theta_2) = (\pi/2, \pi)$, and six-wave mixing (SWM) at $2\Omega_3 - 2\Omega_2 + \Omega_1$ for $\tau_{12} = 0.5$ ps, $\tau_{23} = 1$ ps, $(\theta_1, \theta_2, \theta_3) = (\pi/2, \pi, \pi)$. Integration time 20 s. Heterodyned spectral shape of \mathcal{E}_2 is shown with a purple, dashed line. b) Amplitude of the FWM hyperspectral imaging at $\tau_{12} = 1$ ps. Localized peaks correspond to the FWM of single QDs: the amplitude is displayed as brightness, the energy is indicated as the hue of the colour range (indicated by the bar) from -0.3 (red) to +0.3 meV (blue) with respect to the chosen center of $\hbar\omega = 1350$ meV. c) Population dynamics (brown squares) of the trion probed with FWM, $\tau_{12} = 0.5$ ps: exponential decay (brown line) yields the population lifetime of $T_1 = (390 \pm 10)$ ps. Coherence dynamics (black circles) of the same trion probed with FWM, consistent with radiatively limited dephasing $T_2 = 2T_1$ and a residual inhomogeneous broadening of $\sigma = (3 \pm 1) \mu\text{eV}$. d) FWM power as a function of $\sqrt{P_1} = |\mathcal{E}_1|$ and of \mathcal{E}_1 pulse area θ_1 showing Rabi oscillations, $\theta_2 = 2/3\pi$, $P_2 = |\mathcal{E}_2|^2 = 157 \text{ W/cm}^2$, $\tau_{12} = 0.5$ ps. Pulse areas of $(\theta_1, \theta_2) = (\pi/2, \pi)$, corresponding to $(P_1, P_2) = (72, 235) \text{ W/cm}^2$, are determined by the first maximum of the FWM versus θ_1 (θ_2 , not shown). Predicted $\sin^2(\theta_1) \exp(-\xi\theta_1)$ is depicted by the orange dashed-dotted line, where ξ is the damping constant.

frequency, while varying the delay τ_{23} between \mathcal{E}_2 and \mathcal{E}_3 and fixing $\tau_{12} = 0.5$ ps. The resulting evolution of the FWM amplitude is shown in Fig. 1c and fitted by an exponential decay, yielding^{22,23} the lifetime of $T_1 = (390 \pm 10)$ ps. Conversely, detecting the FWM at the frequency $2\Omega_2 - \Omega_1$, reflects the coherence in the TLS. Its evolution is governed by the delay τ_{12} between \mathcal{E}_1 and \mathcal{E}_2 , as displayed in Fig. 1c. The lack of FWM at negative delays and the absence of fine-structure beating¹⁹ confirm the tri-

onic nature of the investigated transition. Our data are well described by the product of an exponential and a Gaussian decay¹⁹. From the former, we infer the dephasing time T_2 and the related homogenous broadening $\gamma_2 = 2\hbar/T_2$ (FWHM). The latter yields the inhomogeneous broadening σ due to the residual spectral wandering, occurring during the integration time. Note that even on the single transition level such wandering creates a photon echo, manifested here by a Gaussian decay of the coherence^{19,24}. The coherence dynamics can be fitted using $T_2 = 2T_1 = 780$ ps and $\sigma = (3 \pm 1) \mu\text{eV}$. We thus find that the coherence of trions in these QDs approaches the radiative limit. This is supported by observation of their first order reflectance, as shown in Supplementary Fig. S5. More examples of such transitions close to the radiative limit are given in Supplementary Fig. S4.

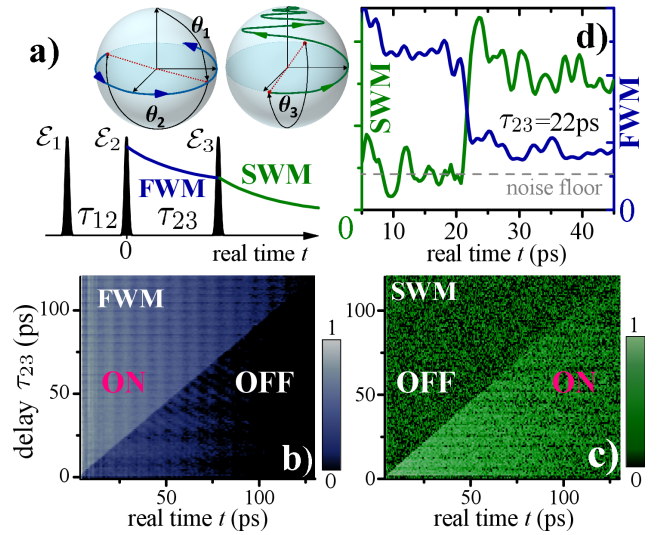


FIG. 2. FWM/SWM switching. a) Pulse sequence used in the experiment, highlighting rationale of the FWM/SWM switching. The evolution of the trion's Bloch vector (red) during FWM, switching and SWM is also depicted (ground state on the top of the sphere). The FWM transient (blue line) is created by \mathcal{E}_1 and \mathcal{E}_2 fields arriving at $t = -\tau_{12}$ and $t = 0$, respectively and it freely evolves during τ_{23} . \mathcal{E}_3 , arriving at $t = \tau_{23}$, converts the FWM into the SWM (green line). The FWM/SWM conversion efficiency reaches unity for $\theta_3 = \pi$. FWM (b) and SWM (c) amplitudes as a function of real time t and delay τ_{23} for $\theta_3 = 0.8\pi$. FWM (SWM) signals are present above (below) the diagonal giving the arrival of \mathcal{E}_3 . Amplitude on a linear colour scale, as given. Decreased amplitudes for long times is due to the limited resolution of the spectrometer. d) Demonstration of the FWM suppression (blue) and the SWM build up (green trace) at the arrival of \mathcal{E}_3 for $t = \tau_{23} = 22$ ps. The noise floor is given by a gray dashed line. Note the coexistence of both signals for $t > 22$ ps and corresponding residual signal in Fig. 3c, owing to $\theta_3 \neq \pi$.

The coherent control experiment described below requires a calibration of the pulse areas $\theta_i = \int dt \mu |\mathcal{E}_i(t)| / \hbar$, which are proportional to the square root of the pulse intensities P_i . To illustrate this calibration, we present in Fig. 1d the FWM power as a function of $\sqrt{P_1}$ and θ_1 . As expected^{16,25,26}, the FWM undergoes Rabi oscillations with increasing θ_1 . In addition, we observe a θ_1 -dependent damp-

ing, which is attributed to dissipative coupling with acoustic phonons²⁷. In the three-beam heterodyne spectral interferometry technique, the additional degree of freedom provided by the time delay τ_{23} allows to transform the FWM into SWM at the defined time after creating the FWM. Such SWM signals and their interferences with coexisting FWM have been studied in atomic physics^{28,29}. Higher order wave-mixing has been also investigated in the condensed matter physics to explore many particle correlations in quantum wells^{30–32} and QD ensembles³³, recently inferring their non-Markovian dynamics³⁴. In the present study, we demonstrate for the first time generation of SWM on single emitters. Here, SWM detection serves as a tool to implement coherent control upon the FWM transient of a TLS. We use \mathcal{E}_3 pulse to project the FWM into the SWM signal oscillating at the $2\Omega_3 - 2\Omega_2 + \Omega_1$ frequency. The spectral interferogram measured at this frequency is shown in Fig. 1a, for the applied pulse sequence given in Fig. 2a. The FWM/SWM swapping is controlled by adjusting the pulse area θ_3 and τ_{23} , as derived in the analytical model presented in the Supplementary Material: FWM field \mathcal{E}_f and SWM field \mathcal{E}_s read:

$$|\mathcal{E}_f(t)| \propto \sin \theta_1 \sin^2 \frac{\theta_2}{2} \left(\Theta(t) - \sin^2 \frac{\theta_3}{2} \Theta(t - \tau_{23}) \right) \times e^{-t\gamma_2}, \quad (1)$$

$$|\mathcal{E}_s(t)| \propto \sin \theta_1 \sin^2 \frac{\theta_2}{2} \sin^2 \frac{\theta_3}{2} \Theta(t - \tau_{23}) e^{-t\gamma_2}, \quad (2)$$

where Θ is the Heaviside function, and $t = 0$ is defined by the arrival of \mathcal{E}_2 .

Conversion of FWM into SWM and their coexistence is experimentally demonstrated in Fig. 2. Therein, we present the FWM and SWM field amplitude transients for increasing τ_{23} at $\theta_3 = 0.8\pi$. In such maps, the arrival of \mathcal{E}_3 at $t = \tau_{23}$, generating the conversion, defines the diagonal. From Eqs. (1) and (2), we expect that the FWM is present in the upper-side of the diagonal ($t < \tau_{23}$), and has been converted to SWM in the lower-side ($t > \tau_{23}$), as indeed measured. This temporal gating of both signals is the key to manipulate the spectral distribution of the FWM from a TLS.

We note that the conversion efficiency reaches unity for the $\theta_3 = \pi$ yielding, at the arrival of \mathcal{E}_3 , a complete suppression of the FWM. In Fig. 3, we employ specific pulse areas $(\theta_1, \theta_2) = (\frac{\pi}{2}, \pi)$ in order to drive, between \mathcal{E}_2 and \mathcal{E}_3 , the maximum polarization to the FWM, consistent with Eq. (1). In Fig. 3a we present FWM transients measured at $\theta_3 = \pi$ for various τ_{23} . Their spectral amplitudes (also see Supplementary Fig. S6) are given in Fig. 3b. The spectra show a substantial broadening and ringing due to the step-like suppression in time, leading to a sine cardinal like shape. FWM at $\theta_3 = 0$ (topmost) is given for comparison. The effect, also clearly visible in Fig. 3c, is observable from $\tau_{23} = 110$ ps to $\tau_{23} = 10$ ps where the FWHM of the main peak increases from $38 \mu\text{eV}$ (given by the spectral resolution) up to $700 \mu\text{eV}$. This represents an imposed broadening by two orders of magnitude with respect to γ_2 . With further decrease of τ_{23} such spectral broadening can reach 10 meV range, as is only

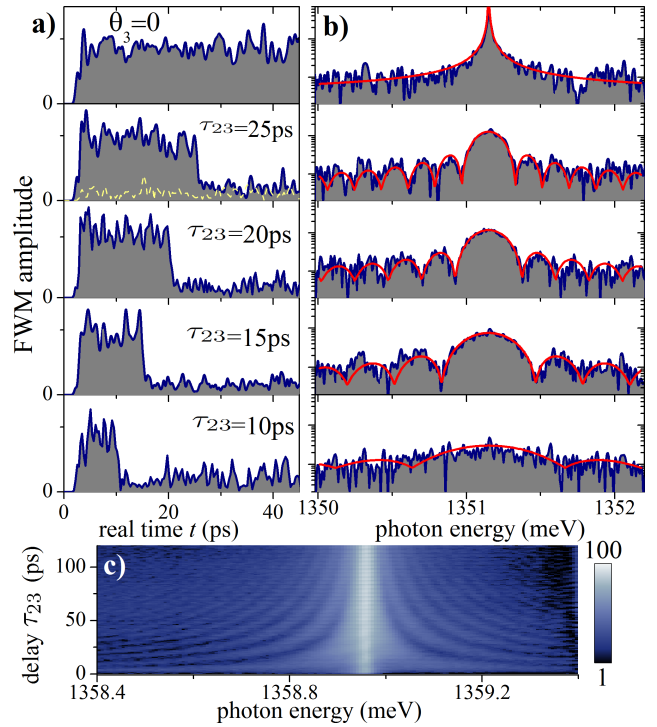


FIG. 3. Manipulation of the coherent response of a single emitter via wave-mixing switching. a) FWM transients generated for $\tau_{12} = 0.2$ ps, $\theta_3 = \pi$ and τ_{23} as labeled. A complete suppression of the FWM is observed after the arrival of \mathcal{E}_3 ($t > \tau_{23}$); the noise level is shown by the dashed yellow line. The free evolution of the FWM for $\theta_3 = 0$ is shown in the topmost panel. b) FWM spectral amplitudes of the data in a), showing a substantial spectral broadening of the FWM due to the step-like suppression of the signal in time domain. Analytical predictions using Eq. (14) are shown as red lines. c) FWM spectral amplitudes of the transients given in Fig. 2b, showing the evolution of the FWM lineshape with increasing τ_{23} for $\theta_3 = 0.8\pi$. Logarithmic colour scale, as shown by the vertical bar.

bounded by the duration of \mathcal{E}_3 . Due to the limited amount of the emitted FWM for $\tau_{23} \simeq 0$, its observation requires a large signal-to-noise ratio. Fourier transforming Eq. (1) with respect to the real time t , yields the spectrally resolved FWM amplitude:

$$|\mathcal{E}_f(\omega)| \propto \sin \theta_1 \sin^2 \frac{\theta_2}{2} e^{-\tau_{12}\gamma_2} \times \left(\frac{1 + \sin^4 \frac{\theta_3}{2} e^{-2\tau_{23}\gamma_2} - 2 \sin^2 \frac{\theta_3}{2} e^{-\tau_{23}\gamma_2} \cos \Delta\omega\tau_{23}}{2\pi(\gamma_2^2 + \Delta\omega^2)} \right)^{1/2} \quad (3)$$

where $\Delta\omega = \omega - \omega_{eg}$. With the particular pulse areas $(\theta_1, \theta_2, \theta_3) = (\frac{\pi}{2}, \pi, \pi)$, the spectrum takes the simple form $e^{-\gamma_2(\tau_{12} + \tau_{23})} \left(\frac{\cosh(\gamma_2\tau_{23}) - \cos(\Delta\omega\tau_{23})}{\pi(\gamma_2^2 + \Delta\omega^2)} \right)^{1/2}$, which reproduces the observed features quantitatively, as shown by red traces in Fig. 3b. The spectral broadening of the central peak scales as $\frac{2\pi\hbar}{\tau_{23}}$, characteristic of the sine cardinal lineshape.

For intermediate values of θ_3 , the FWM is only partially converted to SWM. Therefore both nonlinearities coexist, as can be noted in Fig. 2d. This is

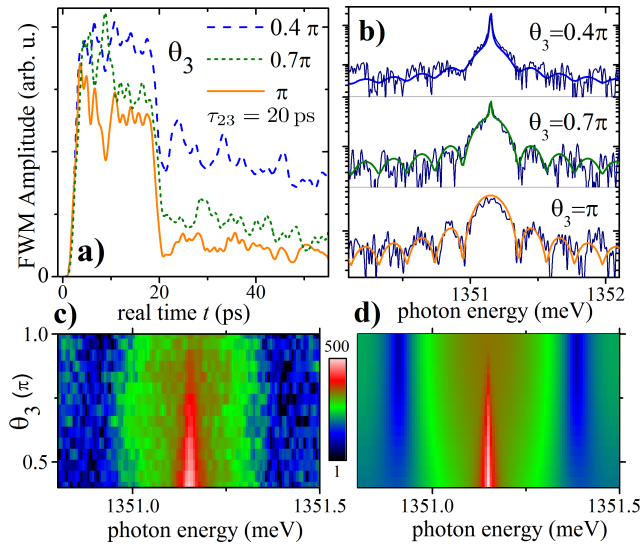


FIG. 4. **Manipulation of the FWM with the area of the control pulse \mathcal{E}_3 .** a) Measured evolution of the FWM transient for θ_3 of 0.4π (blue dashed), 0.7π (green dotted) and π (orange solid); for $\tau_{12} = 0.2$ ps and $\tau_{23} = 20$ ps. An increasing suppression of the FWM for $t > \tau_{23}$ with increasing θ_3 is observed. b) FWM spectral amplitudes of the transients shown in a), with the corresponding theoretical prediction according to Eq. (3). c) Map of the FWM spectral amplitude as a function of θ_3 demonstrating a gradual suppression of the spectrally narrow component of the FWM. Delays as in a). d) Theoretical simulation of c). Logarithmic color scale, as shown with the colour bar.

investigated in Fig. 4, where the FWM transients (a) and spectra (b) for increasing θ_3 and fixed $\tau_{23} = 20$ ps are presented. Owing to the increasing FWM suppression for $t > 20$ ps, the amplitude of the spectrally narrow component is reduced (see Supplementary Fig. S7). In parallel, the broad pedestal develops. Hence, non-natural lineshapes can be designed by tuning θ_3 and τ_{23} . Eq. (14), derived in the Supplementary Material, reproduces the experimental data shown in Fig. 4 b and c, without any free parameters, apart from the absolute common scaling.

The ability to manipulate the spectral width of a coherent response from the TLS provides a novel degree of freedom in solid state quantum optics. We emphasize that the phase shift induced by the FWM/SWM conversion modifies the coherent oscillation of the

dipole: the global lineshape of the TLS polarization is altered, as highlighted in Supplementary Fig. S8. The latter is strikingly manifested when the \mathcal{E}_3 is heterodyned at $2\Omega_2 - \Omega_1$, leading to a stationary phase shift between the two non-linearities generated by \mathcal{E}_2 and \mathcal{E}_3 , respectively. Therefore by adjusting this phase shift with τ_{23} (see Eqs. (11) and (12) in the Supplementary Material), we can perform controlled phase rotations of the TLS dipole. After arrival of \mathcal{E}_3 , the phase of the TLS emission could be inverted or entirely frozen. Such on-demand blockade of emission represents a fundamental step in optical control of single TLS systems. As an example of application, let us note that tuning the spectral shape of a TLS could be employed to optimize injection and storing of single photons in optical resonators. Furthermore, maximizing the spectral overlap within a pair of distant TLSs promotes their coherent coupling via propagating photons³⁵, which is a prerequisite to realize optically controlled quantum networks in a solid. Multi-wave mixing could be also used to selectively address the coherence dynamics and transitions in higher manifolds of the Jaynes-Cummings ladder of nanophotonic devices operating in a strong-coupling regime^{11,17}.

By employing a low-Q semiconductor microcavity, we improved the retrieval sensitivity of coherent responses from individual emitters, enabling wave mixing spectroscopy of individual excitons in strongly-confined InAs QDs. Using three beam configuration, we inferred a new scheme for controlling coherent evolution of a TLS via converting FWM to SWM. We have demonstrated that, via temporal gating of the FWM, we can control its lineshape by varying the amplitude and the arrival time of the gate pulse. The demonstration of SWM on individual emitters paves the way towards investigations of their non-Markovian dynamics³⁴ and to study higher order correlations³⁰ involving more than two excitons within a QD. Extending our proof-of-principle protocol toward control via multi-wave mixing is conceptually straightforward: conversion between wave mixing processes is determined by areas and respective delays of driving pulses. It is also technically feasible via multiplexed digital heterodyning. An alluring perspective is to perform multi-wave mixing on radiatively coupled pairs of distant excitons³⁵, achieving non-local quantum control in a solid.

We acknowledge support by the European Research Council Starting Grant “PICSEN” contract no. 306387.

* francois.fras@ipcms.unistra.fr

† jacek.kasprzak@neel.cnrs.fr

¹ Pla, J. J. *et al.* High-fidelity readout and control of a nuclear spin qubit in silicon. *Nature* **496**, 334–338 (2013).

² Muhonen, J. T. *et al.* Storing quantum information for 30 seconds in a nanoelectronic device. *Nat. Nanotechnol.* **9**, 986–991 (2014).

³ Widmann, M. *et al.* Coherent control of single spins in silicon carbide at room temperature. *Nature Mater.*

14, 164–168 (2015).

⁴ Yale, C. G. *et al.* All-optical control of a solid-state spin using coherent dark states. *Proc. Natl. Acad. Sci. U.S.A.* **110**, 7595–7600 (2013).

⁵ Carter, S. G. *et al.* Quantum control of a spin qubit coupled to a photonic crystal cavity. *Nature Photon.* **7**, 329–334 (2013).

⁶ Hansom, J. *et al.* Environment-assisted quantum control of a solid-state spin via coherent dark states. *Nature Phys.* **10**, 725–730 (2014).

- ⁷ Borri, P. *et al.* Ultralong dephasing time in InGaAs quantum dots. *Phys. Rev. Lett.* **87**, 157401 (2001).
- ⁸ Langbein, W. & Patton, B. Heterodyne spectral interferometry for multidimensional nonlinear spectroscopy of individual quantum systems. *Opt. Lett.* **31**, 1151 (2006).
- ⁹ Vandersypen, L. M. K. & Chuang, I. L. NMR techniques for quantum control and computation. *Rev. Mod. Phys.* **76**, 1037 (2005).
- ¹⁰ Reithmaier, J. P. *et al.* Strong coupling in a single quantum dot-semiconductor microcavity system. *Nature* **432**, 197–200 (2004).
- ¹¹ Albert, F. *et al.* Microcavity controlled coupling of excitonic qubits. *Nature Comm.* **4**, 1747 (2013).
- ¹² Luxmoore, I. J. *et al.* Interfacing spins in an InGaAs quantum dot to a semiconductor waveguide circuit using emitted photons. *Phys. Rev. Lett.* **110**, 037402 (2013).
- ¹³ Coles, R. J. *et al.* Waveguide-coupled photonic crystal cavity for quantum dot spin readout. *Opt. Express* **22**, 2376–2385 (2014).
- ¹⁴ Reichert, T. *et al.* Highly directed emission from self-assembled quantum dots into guided modes in disordered photonic-crystal waveguides. *Phys. Rev. B* **90**, 115310 (2014).
- ¹⁵ Arcari, M. *et al.* Near-unity coupling efficiency of a quantum emitter to a photonic crystal waveguide. *Phys. Rev. Lett.* **113**, 093603 (2014).
- ¹⁶ Patton, B., Woggon, U. & Langbein, W. Coherent control and polarization readout of individual excitonic states. *Phys. Rev. Lett.* **95**, 266401 (2005).
- ¹⁷ Kasprzak, J. *et al.* Up on the Jaynes-Cummings ladder of a quantum-dot/microcavity system. *Nat. Mater.* **9**, 304–308 (2010).
- ¹⁸ Kasprzak, J., Patton, B., Savona, V. & Langbein, W. Coherent coupling between distant excitons revealed by two-dimensional nonlinear hyperspectral imaging. *Nat. Phot.* **5**, 123 (2011).
- ¹⁹ Kasprzak, J. *et al.* Vectorial nonlinear coherent response of a strongly confined exciton-biexciton system. *New J. Phys.* **15**, 055006 (2013).
- ²⁰ Maier, S. *et al.* Bright single photon source based on self-aligned quantum dot-cavity systems. *Optics Ex.* **22**, 8136 (2014).
- ²¹ Benny, Y. *et al.* Excitation spectroscopy of single quantum dots at tunable positive, neutral, and negative charge states. *Phys. Rev. B* **86**, 085306 (2012).
- ²² Langbein, W. *et al.* Radiatively limited dephasing in InAs quantum dots. *Phys. Rev. B* **70**, 033301 (2004).
- ²³ Proux, R. *et al.* Measuring the photon coalescence time window in the continuous-wave regime for resonantly driven semiconductor quantum dots. *Phys. Rev. Lett.* **114**, 067401 (2015).
- ²⁴ Patton, B., Langbein, W., Woggon, U., Maingault, L. & Mariette, H. Time- and spectrally-resolved four-wave mixing in single CdTe/ZnTe quantum dots. *Phys. Rev. B* **73**, 235354 (2006).
- ²⁵ Bonadeo, N. H. *et al.* Coherent optical control of the quantum state of a single quantum dot. *Science* **282**, 1473 (1998).
- ²⁶ Stievater, T. H. *et al.* Rabi oscillations of excitons in single quantum dots. *Phys. Rev. Lett.* **87**, 133603 (2001).
- ²⁷ Ramsay, A. *et al.* Phonon-induced Rabi-frequency renormalization of optically driven single InGaAs/GaAs quantum dots. *Phys. Rev. Lett.* **105**, 177402 (2010).
- ²⁸ Zhang, Y., Brown, A. W. & Xiao, M. Observation of interference between four-wave mixing and six-wave mixing. *Optics Lett.* **32**, 1120 (2007).
- ²⁹ Zhang, Y., Khadka, U., Anderson, B. & Xiao, M. Temporal and spatial interference between four-wave mixing and six-wave mixing channels. *Phys. Rev. Lett.* **102**, 013601 (2009).
- ³⁰ Turner, D. & Nelson, K. Coherent measurements of high-order electronic correlations in quantum wells. *Nature* **466**, 1089–1092 (2010).
- ³¹ Axt, V. M., Bolton, S. R., Neukirch, U., Sham, L. J. & Chemla, D. S. Evidence of six-particle coulomb correlations in six-wave-mixing signals from a semiconductor quantum well. *Phys. Rev. B* **63**, 115303 (2001).
- ³² Voss, T. *et al.* Biexcitonic effects in the coherent control of the excitonic polarization detected in six-wave-mixing signals. *Phys. Rev. B* **66**, 155301 (2002).
- ³³ Moody, G. *et al.* Fifth-order nonlinear optical response of excitonic states in an InAs quantum dot ensemble measured with two-dimensional spectroscopy. *Phys. Rev. B* **87**, 045313 (2013).
- ³⁴ Tahara, H., Ogawa, Y., Minami, F., Akahane, K. & Sasaki, M. Long-time correlation in non-markovian dephasing of an exciton-phonon system in InAs quantum dots. *Phys. Rev. Lett.* **112**, 147404 (2014).
- ³⁵ Minkov, M. & Savona, V. Radiative coupling of quantum dots in photonic crystal structures. *Phys. Rev. B* **87**, 125306 (2013).

SUPPLEMENTARY MATERIAL

Multi-Wave Coherent Control of a Solid State Single Emitter

F. Fras, Q. Mermillod, G. Nogues, C. Hoarau, C. Schneider,
M. Kamp, S. Höfling, W. Langbein, and J. Kasprzak

I. THEORY: DERIVATION OF THE FWM AND SWM RESPONSES

In this part we derive the four-wave mixing (FWM) and six-wave mixing (SWM) responses, as experimentally studied in the main part of the manuscript. We consider a two level system (TLS) formed by an electron in the ground state $|0\rangle$ and a trion in the excited state $|1\rangle$. In the model developed below the coupling between the optical fields and the TLS is treated exactly. The optical response of the TLS is expressed at all orders of the exciting field amplitudes (not limited to the third and five orders, which are usually considered in the low field intensity regime). The relevant semiclassical Hamiltonian of the considered system in interaction with the three exciting fields is given by $H = H_0 + H_L$,

$$H_0 = \hbar\omega_{eg}|1\rangle\langle 1|,$$

$$H_L = \sum_{i=1}^3 \mu \mathcal{E}_i(t) e^{i(\omega_{eg}(t-\tau_i)+\phi_i)}|0\rangle\langle 1| + \text{c.c.}, \quad (4)$$

where ω_{eg} refers to the electron-trion optical transition frequency, μ is the electric dipole of the QD, $\mathcal{E}_i(t)$ determines the effective electric field amplitude of the pulse i at the QD position, τ_i represents the arrival time of the pulse i at the QD position and ϕ_i refers to the additional phase shift induced by optical heterodyning. The excitation pulses are assumed to be delta-function pulses, i.e., $\mathcal{E}_i(t) = \mathcal{E}_i\delta(t - \tau_i)$. In addition to the evolution governed by the Hamiltonian H , the system undergoes dissipative dynamics due to the coupling with its environment. Therefore the state of the system $\rho(t)$ is described in the density matrix formalism in the basis $\{|0\rangle, |1\rangle\}$.

In order to relate the different multi-wave responses we derive the state of the system $\rho(t)$. We assume that the pulse duration is much shorter than the relevant time scales of the system dynamics. Therefore the interaction between the system and its dissipative environment is neglected during the coupling with the optical excitation fields. Under this assumption, the modification of the state $\rho(t)$ induced by the pulses is obtained analytically^{36,37} according to the unitary transformation $U(\theta)$:

$$\rho(\tau_i^+) = U(\theta_i)\rho(\tau_i^-)U(\theta_i)^\dagger, \quad (5)$$

$$U(\theta_i) = \cos \frac{\theta_i}{2} [|0\rangle\langle 0| + |1\rangle\langle 1|] - i \sin \frac{\theta_i}{2} [|0\rangle\langle 1| e^{i(\phi_i - \omega_{eg}\tau_i)} + \text{c.c.}], \quad (6)$$

where $\tau_i^{-(+)}$ denotes the time instant just before (after) the pulse i , and $\theta_i = \int_{-\infty}^{+\infty} dt \mu \mathcal{E}_i(t) / \hbar$ is the area of the pulse i . During the delay time between the pulses the open two-level system relaxes its density and polarization.

In the following the dissipation is described in the Markov limit, the subsequent dynamics can be then given by a master equation in the Lindblad form

$$\dot{\rho} = -\frac{i}{\hbar}[H_0, \rho] + \mathcal{L}(\rho) \quad (7)$$

where \mathcal{L} is the superoperator of dissipation. It takes into account the dissipation of energy (mainly induced by spontaneous emission in our experimental case) and pure dephasing processes, which are characterized respectively by the rates γ_1 and γ_d . Given the minute values of fluctuations induced by the spectral wandering (as measured in Fig. 1. c), the inhomogeneous dephasing is disregarded here. Therefore \mathcal{L} reads as:

$$\mathcal{L}(\rho) = \gamma_1 [C\rho C^\dagger - \frac{1}{2}\{C^\dagger C, \rho\}_+] + \frac{1}{2}\gamma_d [D\rho D - \frac{1}{2}\{D^2, \rho\}_+] \quad (8)$$

with $C = |1\rangle\langle 0|$ and $D = |1\rangle\langle 1| - |0\rangle\langle 0|$.

By solving this equation we derive the complete optical polarization dynamics, which is proportional to the off-diagonal terms of the density matrix. We deduce therefore the field \mathcal{E}_{QD} radiated by the quantum dot structure:

$$\mathcal{E}_{QD}(t) = A \langle 1 | \rho(t) | 0 \rangle + \text{c.c.} \text{ with } A = i\mu_0 c \omega_{eg} \mu \kappa \quad (9)$$

where κ represents a coefficient of proportionality including phase shift and absorption due to the propagation inside the structure.

The coherent optical response of the QD can be developed in a sum of contributions $\mathcal{E}_{\mathbf{n}}$, referring to particular nonlinear processes. The emitted fields $\mathcal{E}_{\mathbf{n}}$ are identified by their phase factors $e^{i\phi_{\mathbf{n}}}$, where the phase $\phi_{\mathbf{n}}$ results from a linear combination of the exciting pulse phases : $\phi_{\mathbf{n}} = \sum_i a_i \phi_i$ and $\mathbf{n} = \{a_1, a_2, a_3\} \in \mathbb{Z}^3$.

The principle of the heterodyne spectral interferometry experiment is based on the capacity to select a specific $\mathcal{E}_{\mathbf{n}}$ via corresponding phase $\phi_{\mathbf{n}}$. To do so, the phase relation between the exciting pulses is tailored by acousto-optics modulators operating at radio-frequencies Ω_i . Therefore successive exciting pulses $\{\mathcal{E}_i\}$ belonging to optical train i , characterized by a repetition rate τ_r , are phase shifted by a factor $\Omega_i \tau_r$. By repeating the experiment in time and combining optical heterodyning with the spectral interferometry we retrieve the amplitude and phase of the desired non-linear component $\mathcal{E}_{\mathbf{n}}$ out from the total electric field radiated by the QD dipole⁸. In the present study, the nonlinear signals of interest are the following :

- the non-degenerate FWM $\mathcal{E}_{\mathbf{f}'}$ beating at the heterodyne frequency $\phi_{\mathbf{f}'} = \phi_3 - \phi_2 + \phi_1$
- the degenerate FWM $\mathcal{E}_{\mathbf{f}}$ beating at the heterodyne frequency $\phi_{\mathbf{f}} = 2\phi_2 - \phi_1$
- the degenerate SWM $\mathcal{E}_{\mathbf{s}}$ beating at the heterodyne frequency $\phi_{\mathbf{s}} = 2\phi_3 - 2\phi_2 + \phi_1$

Considering the TLS in the ground state at the time τ_1^- , the dynamics of the optical fields are given by :

$$\mathcal{E}_{\mathbf{f}'}(t) = \frac{A}{2} \sin(\theta_1) \sin(\theta_2) \sin(\theta_3) \Theta(t - \tau_{23}) e^{-(t - \tau_{23} + \tau_{12})\gamma_2 - \tau_{23}\gamma_1} e^{i(\omega_{eg}(t - \tau_{23} + \tau_{12}) + \phi_{\mathbf{f}'})} \quad (10)$$

$$\mathcal{E}_{\mathbf{f}}(t) = A \sin(\theta_1) \sin^2\left(\frac{\theta_2}{2}\right) \left(\Theta(t) - \sin^2\left(\frac{\theta_3}{2}\right) \Theta(t - \tau_{23}) \right) e^{-t\gamma_2} e^{i(\omega_{eg}(t - \tau_{12}) + \phi_{\mathbf{f}})} \quad (11)$$

$$\mathcal{E}_{\mathbf{s}}(t) = -A \sin(\theta_1) \sin^2\left(\frac{\theta_2}{2}\right) \sin^2\left(\frac{\theta_3}{2}\right) \Theta(t - \tau_{23}) e^{-t\gamma_2} e^{i(\omega_{eg}(t - 2\tau_{23} + \tau_{12}) + \phi_{\mathbf{s}})}, \quad (12)$$

where $\Theta(t)$ is the Heaviside function, $\gamma_2 = \gamma_1/2 + \gamma_d$ and $(\tau_1, \tau_2, \tau_3) = (-\tau_{12}, 0, \tau_{23})$ with $\tau_{ij} = \tau_j - \tau_i$ and $\tau_{12} > 0$ and $\tau_{23} > 0$. Once Fourier transformed with respect to the time t , the spectrally resolved wave mixing field amplitudes read as :

$$\mathcal{E}_{\mathbf{f}'}(\omega) = \frac{A}{2} \sin(\theta_1) \sin(\theta_2) \sin(\theta_3) \frac{e^{-\tau_{12}\gamma_2 - \tau_{23}\gamma_1}}{\sqrt{2\pi}(\gamma_2 - i\Delta\omega)}, \quad (13)$$

$$\mathcal{E}_{\mathbf{f}}(\omega) = A \sin(\theta_1) \sin^2\left(\frac{\theta_2}{2}\right) \frac{e^{-\tau_{12}\gamma_2} \left(1 - \sin^2\left(\frac{\theta_3}{2}\right) e^{\tau_{23}(i\Delta\omega - \gamma_2)}\right)}{\sqrt{2\pi}(\gamma_2 - i\Delta\omega)}, \quad (14)$$

$$\mathcal{E}_{\mathbf{s}}(\omega) = -A \sin(\theta_1) \sin^2\left(\frac{\theta_2}{2}\right) \sin^2\left(\frac{\theta_3}{2}\right) \frac{e^{-(\tau_{12} + \tau_{23})\gamma_2}}{\sqrt{2\pi}(\gamma_2 - i\Delta\omega)}, \quad (15)$$

where $\Delta\omega = \omega_{eg} - \omega$ and the phases $\phi_{\mathbf{n}}$ are omitted. In the equations (10) and (13), one can note that the amplitude of the non degenerate FWM signal $\mathcal{E}_{\mathbf{f}'}$ is sensitive to both the relaxation of the polarization and density of the TLS. In particular, the expression (13) in the spectral domain highlights that probing the signal $\mathcal{E}_{\mathbf{f}'}$ as a function of the delay times τ_{12} and τ_{23} allows to experimentally determine the characteristic rates γ_1 and γ_2 , respectively (see Fig. 1 in the main manuscript and Supplementary Fig. S4).

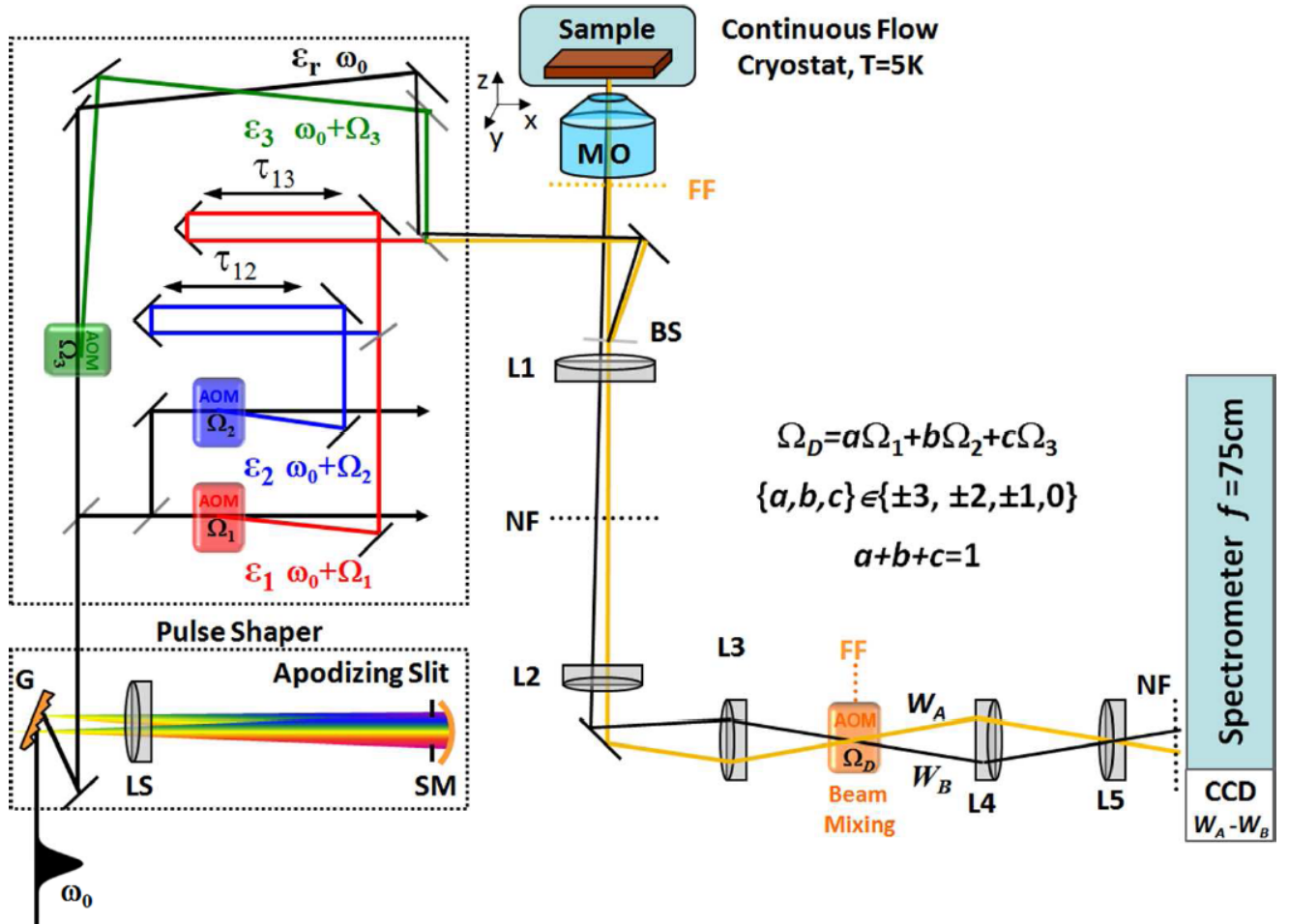
The relations (11) and (12) are describing the core of the experiments presented in the main article. They explicitly illustrate the dynamics of the TLS coherences induced by the third pulse, where the FWM response is projected to the SWM response. This interplay between the two nonlinear processes is controlled by the area θ_3 of the third pulse and the time delay τ_{23} between the last two pulses. Conversely, such degree of freedom permits designing the spectro-temporal shape of the FWM component, as shown in the equations (11, 14).

We point out that the switching between FWM and SWM triggered by \mathcal{E}_3 , physically modifies the coherent oscillation of the dipole and directly acts on the total lineshape of its emission. This is exemplified in Supplementary Figure Fig. S8 (see page 9). Therein, we present simulated spectral lineshape of the complete QD optical polarization after the arrival of the second pulse \mathcal{E}_2 for $(\theta_1, \theta_2, \theta_3) = (\frac{\pi}{2}, \pi, \pi)$. We observe that the spectral lineshape of the dipole is significantly altered (for example for $\tau_{23} = 390$ ps) compared to the unperturbed case ($\theta_3 = 0$). The spectral broadening is generated by the spectral interferences between the FWM (for $t < \tau_{23}$) and SWM (for $t > \tau_{23}$) components, which averaged over many repetitions of the heterodyne experiment produce such spectrum.

II. EXPERIMENTAL DETAILS

Our experiments are based on an extended version of the heterodyne spectral interferometry technique⁸. We use a pulse train spectrally centered at $\hbar\omega_0 = 1.35$ eV, generated by a Ti:Sapphire laser (Spectra-Physics, Tsunami Femto). The pulses are spectrally shaped and chirp-corrected by a passive pulse-shaper (G - grating, LS - lens, SM - spherical mirror). They are then spectrally up-shifted by three acousto-optic modulators

(AOMs) operating at $\Omega_{1,2,3} = (80, 79, 80.77)$ MHz. Thus created three driving fields $\mathcal{E}_{1,2,3}$ - marked as red, blue and green, respectively - acquire relative time delay τ_{13} (positive for \mathcal{E}_1 leading) and τ_{12} (positive for \mathcal{E}_1 leading) by passing through two mechanical delay lines. Their polarization can be controlled by a set of half- and quarter-plates, but in this work we employ co-linear, horizontal (in the lab-frame) polarization for all beams. The driving fields are recombined into the same spatial mode (yellow) and focussed on the sample surface via the microscope objective (MO - Olympus, LCPLN50XIR/0.65, BS beam sampler, FF far field) installed on a X-Y-Z close-loop piezo-stage, (XY-range of $250 \mu\text{m}$, Z- range of $450 \mu\text{m}$). The excitation pulses have duration of 350 ± 50 fs. The pulse chirp, mainly induced by a slab of TeO_2 crystal in the AOMs and in the MO, is compensated by measuring the non-resonant four-wave mixing produced at pulse overlap in an auxiliary GaAs sample and minimizing its duration with respect to τ_{12} . The microcavity sample is installed inside a custom, continuous flow helium cryostat, containing motorized, closed-loop XY translation stages (range of 10 mm, accuracy of 50 nm). Experiments reported here were performed at 5.1 ± 0.1 K. The far field is imaged into the AOM, where - using a Bragg condition - the reflected signal is mixed with the reference field \mathcal{E}_r . The mixing AOM is driven at the frequency $\Omega_D = a\Omega_1 + b\Omega_2 + c\Omega_3$, where $(a, b, c) \in (-3, -2, -1, 0, 1, 2, 3)$ and $a+b+c=1$. These heterodyne frequencies are produced by the home-made three-channel, analogue mixer, with a spectral purity of 40 dB. They are subsequently regenerated by a lock-in amplifier attaining spectral purity of 100 dB. Mixed beams W_A and W_B are imaged into the entrance slit of the imaging spectrometer of 750 mm focal length. Spectral interferograms are retrieved by subtracting and π -phase flipping W_A and W_B , as described in Ref. [8]. We use a CCD camera from Princeton Instruments (PIXIS:400BR eXcelon), offering enhanced full well capacity, readout rate and quantum efficiency of 83% at 915 nm. The wave mixing signal is retrieved in amplitude and phase by performing spectral interferometry and by adjusting \mathcal{E}_r to arrive prior to the signal. We note that we have also tested optical heterodyning by performing digital mixing with an arbitrary wave-form generator (Tektronix, sampling rate 1.2 G/s) and retrieved the FWM from single quantum dots with the same signal-to-noise ratio, as with the analogue mixing. This paves the way towards heterodyne n-wave mixing experiments, enabling quantum control of high order nonlinear processes of individual optical transitions in solids.



Supplementary Figure S1. Schema of the experimental setup.

III. AUXILIARY RESULTS

The sample has been grown by the molecular beam epitaxy. A layer of annealed and capped InAs QDs (density $2 \times 10^9 \text{ cm}^{-2}$) is placed in a center of a GaAs spacer. A δ -doping layer with Si (density $1.8 \times 10^{10} \text{ cm}^{-2}$) is present 10 nm below the QD layer, inducing intentional negative doping of QDs. The spacer is sandwiched between two Bragg mirrors. The bottom (top) mirror contains 24 (5) pairs of $\lambda/4$ $\text{Al}_{0.9}\text{GaAs}/\text{GaAs}$ stacks, forming an asymmetric λ -cavity with a quality factor of $Q \simeq 170$. An example of the micro-photoluminescence hyperspectral imaging frame performed on the studied microcavity is shown in Fig. S2 a. The sample is excited in continuous wave at 1.734 eV with $0.3 \mu\text{W}$ at the sample surface. Blue peaks correspond to the emission of individual InAs quantum dots. Count rates at the peak as high as 10^5 per seconds are routinely detected using a grating of 1800 grooves/mm with Low Noise and gain 2 settings of the Pixis camera. Linear color scale from 0 to 10^5 counts per seconds. In Fig. S2 b we present a typical micro-photoluminescence spectrum (black) and photoluminescence spectrum averaged over $400 \mu\text{m}^2$ (gray). The reflectivity spectrum measured with the white light (blue) shows the cavity mode. The mode is broadened at the high energy side due to high NA of the microscope objective and the in-plane dispersion of the cavity. In Fig. S2 c we present topography of the sample surface, revealed with the atomic force microscopy. Typical topography images over the sample area of $20 \mu\text{m} \times 20 \mu\text{m}$ (left) and of $5 \mu\text{m} \times 5 \mu\text{m}$ are shown, revealing mosaic-like morphology with characteristic oval photonic defects of typically $2 \mu\text{m} \times 1 \mu\text{m}$ in-plane size and of 20 nm high occurring with a spatial density $0.1 \mu\text{m}^{-1}$. Such defects offer an enhanced in- and out-coupling efficiency of around 40 %, as recently shown in Ref. [20]. This, combined with an intra-cavity amplification, results in an enhanced excitation and detection of the coherent nonlinear responses of QDs situated close to the maximum of the localized optical mode induced by a defect. We systematically measure shorter T_1 times (150-350 ps), weaker driving powers and stronger FWM from QDs residing in the defects, with respect to the dots placed outside of defects. We speculate that these observations are due to the change of the photon density of states by the surface modulation defects, creating a varying coupling efficiency and Purcell effect. Further research is required to make a clear assignment and to elucidate the influence of these photonics defects on the coherent response of QDs.

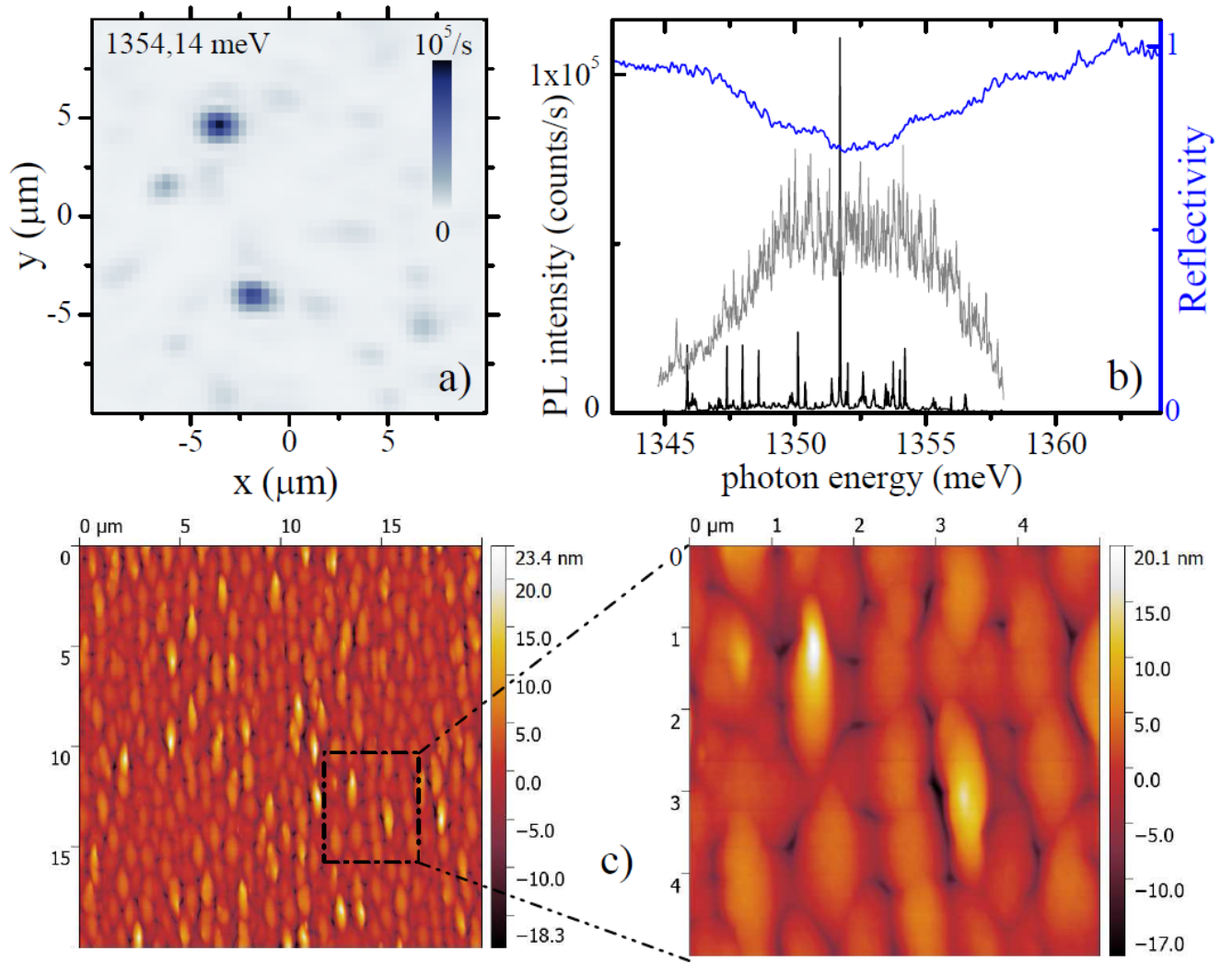
Typical frames of the FWM hyperspectral imaging at $\tau_{12} = +1$ ps and ω as labeled are shown in Fig. S3 a-d. Linear colour scale from black to white, as shown by the vertical bar. Strongest peaks primarily correspond the FWM of negative trions. In order to obtain spectrally-resolved FWM image, as exemplified in Fig. 1 b, the following procedure is applied. For each spatial position, the spectrally-resolved FWM amplitudes are fitted with a Lorentzian function within a chosen energy region (specifically, from 1349.7 meV to 1350.3 meV in Fig. 1 b). The fitted center position yields the energy, while the fitted Lorentzian amplitude is proportional to the FWM amplitude. The retrieved parameters are rearranged into a pair of two-dimensional spatial maps; encoding spectral position and amplitude, respectively. They are finally merged into a single, spatial map, where the amplitude is represented as brightness and the energy as a hue level.

In Fig. S3 e and f we provide the result of the FWM spectral correlation analysis $\Delta C(\delta\omega)$ performed on the hyperspectral imaging FWM data, as defined in Ref. [38]. For $\tau_{12} = +1$ ps, $\Delta C(\delta\omega)$ reveals two peaks at $\delta\omega$ of 2.2 meV and 3.8 meV attributed to neutral exciton and biexciton transitions, present in around 10% of quantum dots. Due to the weak strength of two particle states, specifically negatively charged biexcitons, the FWM of trions is vanishing at negative delays $\tau_{12} < 0$. Therefore for $\tau_{12} = -2$ ps, $\Delta C(\delta\omega)$ shows only one peak at $\delta\omega = 3.6$ meV, attributed to biexciton transitions of neutral excitons. Lower signal to noise ratio is due to smaller statistics available. Wave mixing spectroscopy on such exciton-biexciton-trion systems will be presented in a forthcoming publication.

In Fig. S4 we provide two supplementary FWM measurements performed on two different negative trions, demonstrating their radiatively limited dephasing ($T_2=2T_1$). The population dynamics measured with FWM is shown by brown squares. Fitted mono-exponential decay (brown line) yields population lifetime of $T_1=(400 \pm 7)$ ps (a) and $T_1=(385 \pm 25)$ ps (b). The coherence dynamics measured by FWM is depicted with black circles in (c) and (d), respectively. The data are fitted by the model presented in Ref. [19] (namely Eq. (2)), using radiatively limited dephasing and inhomogeneous broadening due to residual spectral wandering $\sigma = 7 \mu\text{eV}$ (c) and $\sigma = 3 \mu\text{eV}$ (d). Note the initial rise in the coherence dynamics observed in (c), due to the resolved photon echo formation. This figure is supplementary to Fig. 1. Pulse sequences employed to measure coherence (right) and population (left) dynamics are also depicted. The reference pulse \mathcal{E}_r arrives a few ps prior to $t = 0$.

Being radiatively limited, such trions are expected to be observable in the first-order absorption experiment. In Fig. S5 we compare the FWM spectrum (blue line) with a direct reflectance spectrum of the \mathcal{E}_3 beam (black line) measured at the same spot. The FWM reveals dominating transition at 1367.1 meV. The reflectance displays a dip at the same spectral position. It corresponds to the first-order absorption of the QD, with a contrast of a few per-cent resulting from the convolution of the homogenous linewidth with the spectral resolution. To further confirm that the reflectance dip indeed corresponds to the linear absorption of a trion in a single QD, we have performed the pump-probe experiment. The result is given in the inset, where the \mathcal{E}_2 reflectance is shown while increasing the pulse area of the \mathcal{E}_1 beam from $\theta_1 = 0$ (black trace) to $\theta_1 = \pi$ (orange trace) for $\tau_{12} = 2$ ps (\mathcal{E}_1 arriving first). As expected, the \mathcal{E}_2 absorption is gradually decreased with increasing θ_1 and is entirely saturated for the $\theta_1 = \pi$.

In Fig. S6 we present the amplitude of the FWM transient for $\tau_{12} = 0.2$ ps, demonstrating a complete sup-



Supplementary Figure S2. **Sample characterization: micro-photoluminescence, reflectivity and surface topography.**

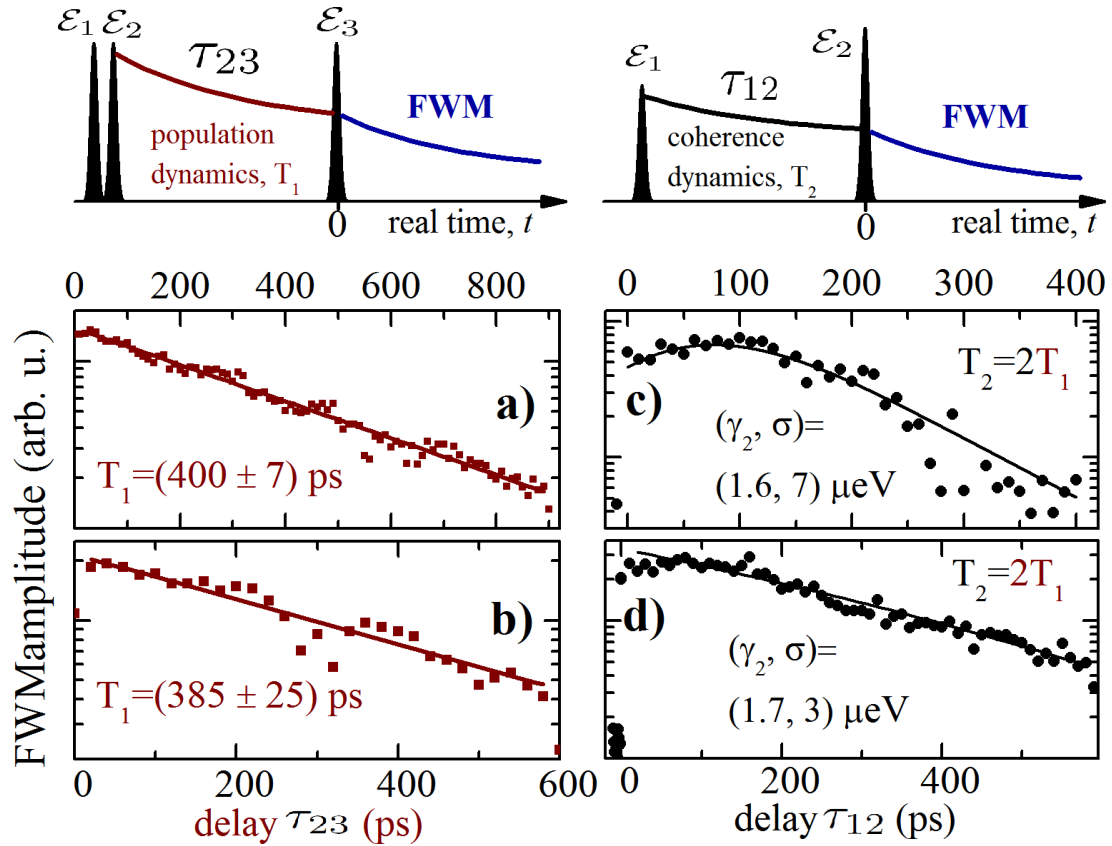
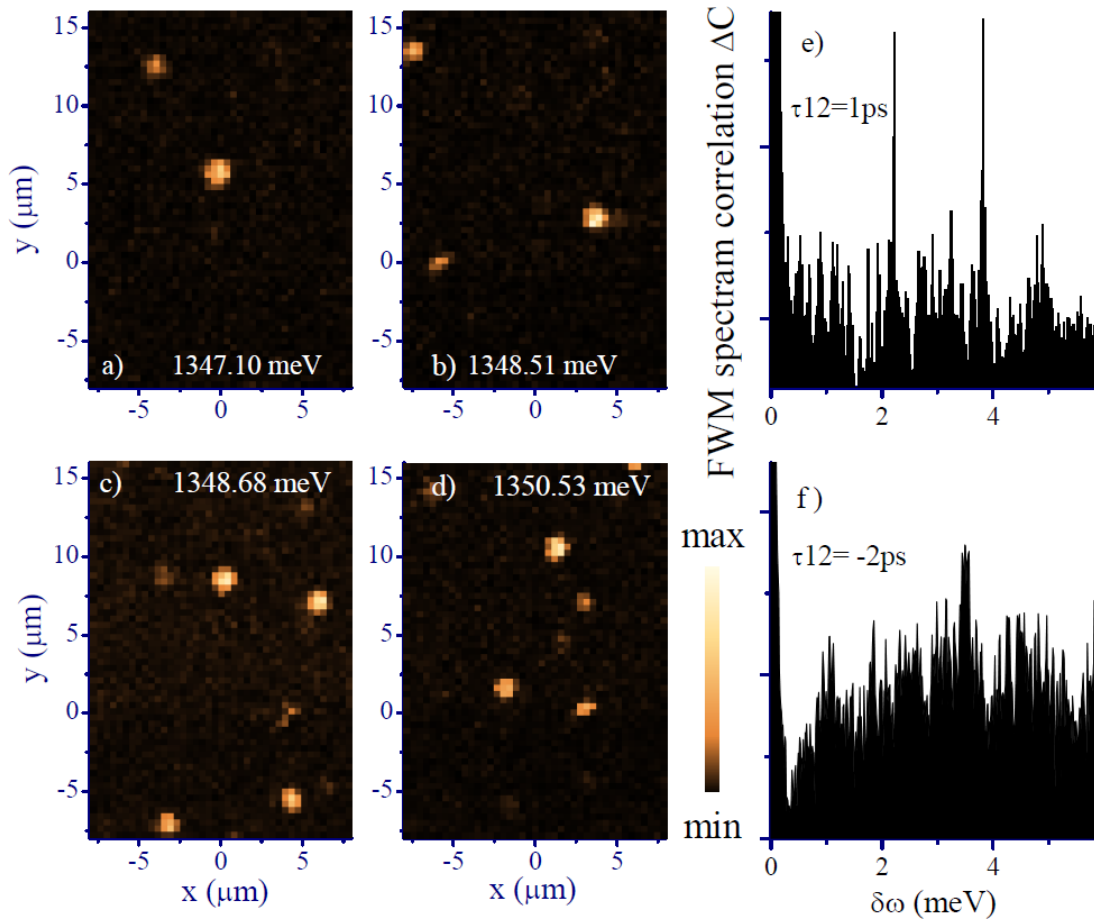
pression of the FWM at the arrival of the \mathcal{E}_3 , which converts the FWM polarization into the SWM one. The pulse area of \mathcal{E}_3 is set to π . Right: Measured FWM spectrum, showing the corresponding change of the FWM spectral lineshape depending on τ_{23} . The data are supplementary to Fig. 3. In Fig. S7, the FWM is generated only within a time window of $\tau_{23} = 6.5$ ps prior to the arrival of \mathcal{E}_3 . As a result, with increasing θ_3 , the FWM gets virtually suppressed. The data are supplementary to Fig. 4.

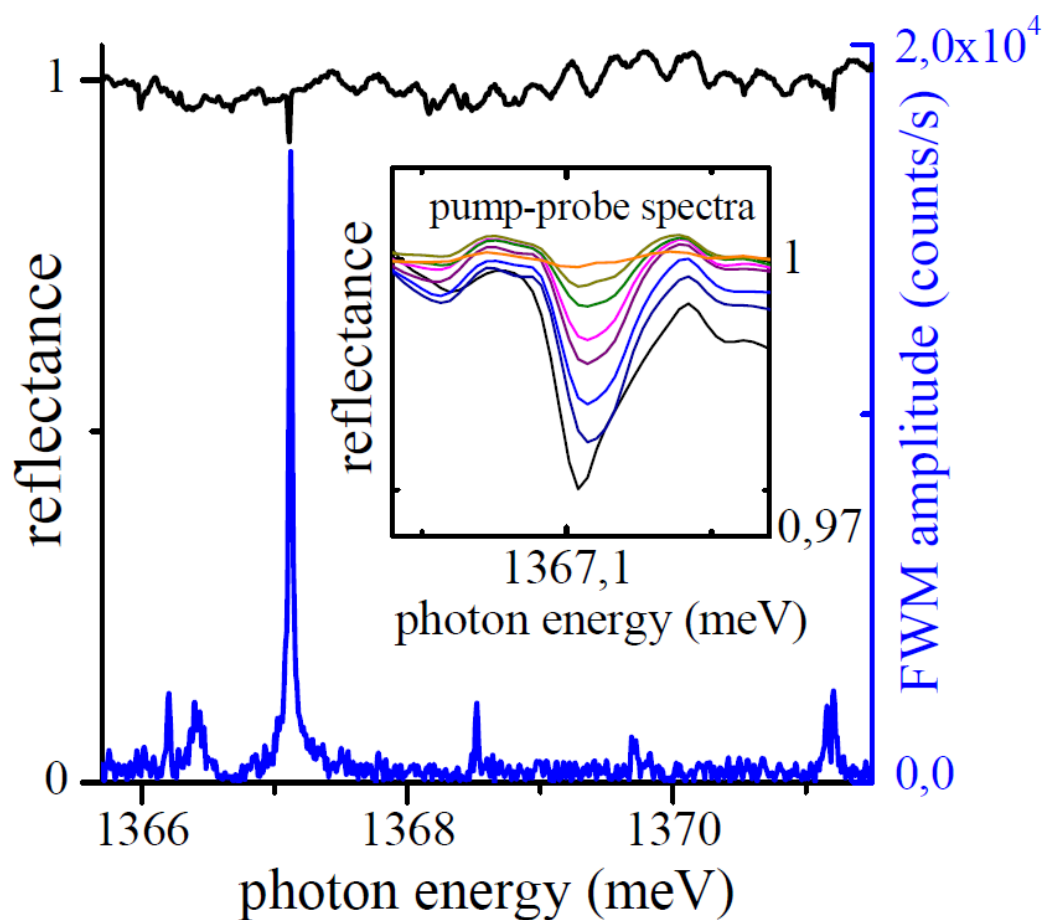
SUPPLEMENTARY REFERENCES

³⁶ A. Bambini and P. R. Berman, Analytic solutions to the two-state problem for a class of coupling potentials *Phys. Rev. A* **23**, 2496 (1981).

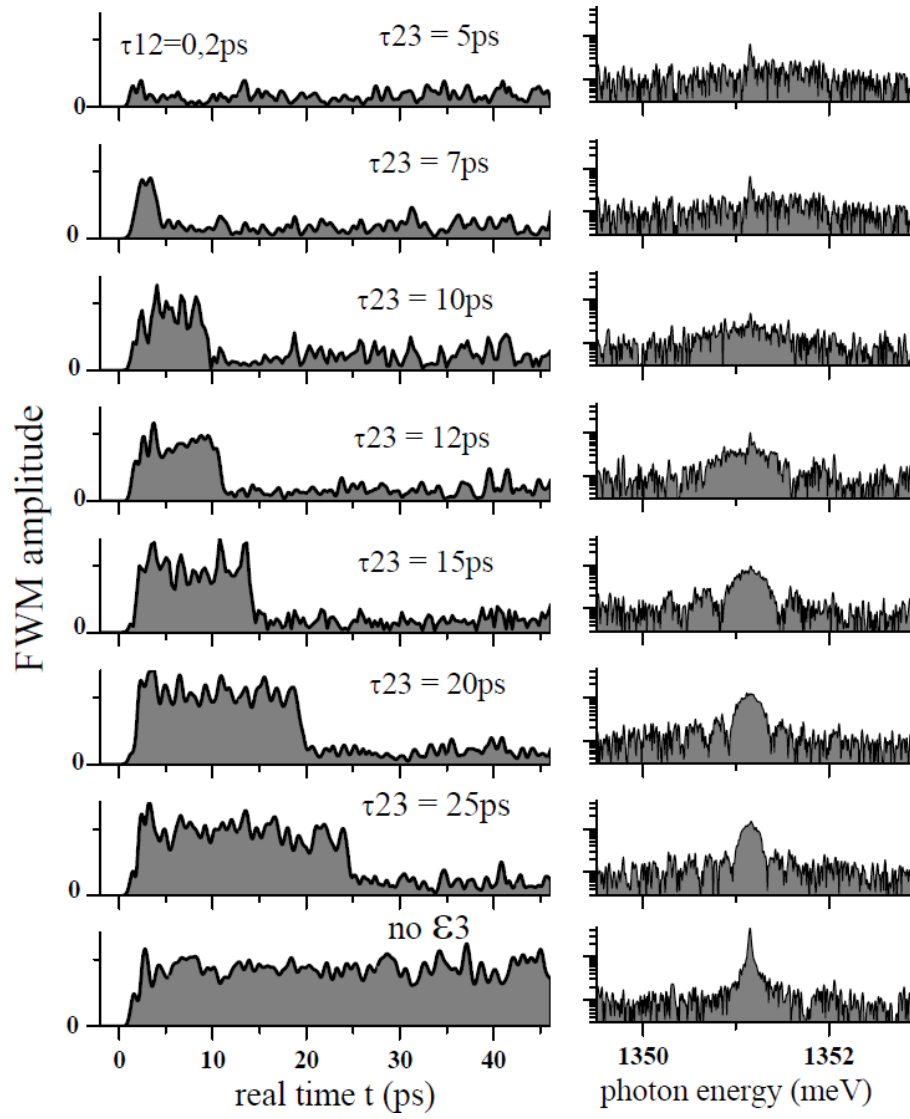
³⁷ Lorenza Viola and Seth Lloyd, Dynamical suppression of decoherence in two-state quantum systems *Phys. Rev. A* **58**, 2733 (1998).

³⁸ J. Kasprzak and W. Langbein, Coherent response of individual weakly confined excitonbiexciton systems *J. Opt. Soc. Am. B* **29**, 1776 (2012).

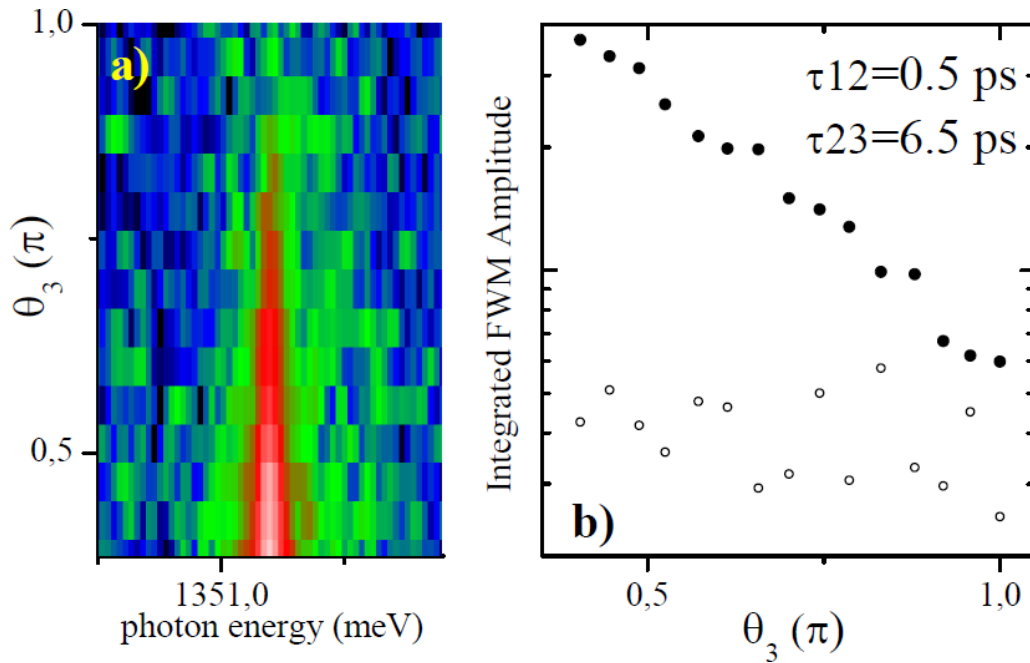




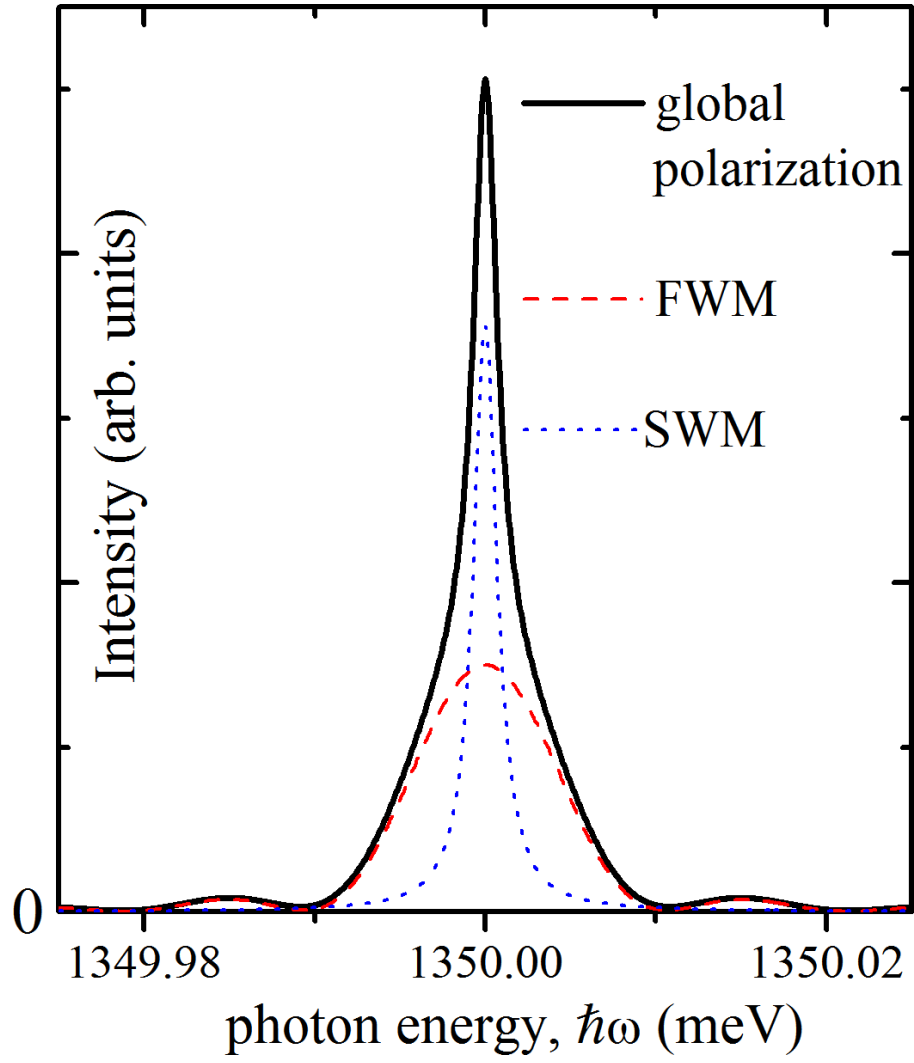
Supplementary Figure S5. Signatures of single triions observed in the direct reflectance and the corresponding pump-probe spectra measured in reflectance.



Supplementary Figure S6. Control of the FWM transient with the delay τ_{23} , between \mathcal{E}_2 of \mathcal{E}_3 .



Supplementary Figure S7. Control of the FWM with the pulse area of \mathcal{E}_3 .



Supplementary Figure S8. **Modification of the global lineshape of a TLS via FWM/SWM switching.** Spectrum of the complete dipole polarization (black solid line) after the arrival of the second pulse \mathcal{E}_2 for $(\theta_1, \theta_2, \theta_3) = (\frac{\pi}{2}, \pi, \pi)$, $T_2 = 780$ ps and $\tau_{23} = 390$ ps. For such value of τ_{23} , the integrated amplitudes of the FWM and SWM components are almost equivalent, which maximizes the spectral interferences between them. FWM (red dashed line) and SWM (blue dotted line) spectra are presented as well.